Nonlinear Dyn
DOI 10.1007/s11071-011-9959-8

ORIGINAL PAPER

Nonlinear resonances in an axially excited beam carrying a top mass: simulations and experiments

R.H.B. Fey · N.J. Mallon · C.S. Kraaij · H. Nijmeijer

Received: 13 September 2010 / Accepted: 17 January 2011
© The Author(s) 2011. This article is published with open access at Springerlink.com

Abstract In this paper, nonlinear resonances in a coupled shaker-beam-top mass system are investigated both numerically and experimentally. The imperfect, vertical beam carries the top mass and is axially excited by the shaker at its base. The weight of the top mass is below the beam's static buckling load. A semi-analytical model is derived for the coupled system. In this model, Taylor-series approximations are used for the inextensibility constraint and the curvature of the beam. The steady-state behavior of the model is studied using numerical tools. In the model with a single beam mode, parametric and direct resonances are found, which affect the dynamic stability of the structure. The model with two beam modes not only shows an additional second harmonic resonance, but also reveals some extra small resonances in the low-frequency range, some of which can be identified as combination resonances. The experimental steady-state response is obtained by performing a (stepped) frequency sweep-up and sweep-down with respect to the harmonic input voltage of the amplifier-shaker combination. A good correspondence between the numerical and experimental steady-state responses is obtained.

Keywords Nonlinear resonances · Dynamic buckling · Beam with top mass · Parametric excitation · Bifurcations · Nonlinear mode interaction · Experiments

1 Introduction

The function of many structures in engineering practice is to carry a static load. To minimize costs, it is often desired to reduce the mass of the supporting structure as much as possible, while retaining a high stiffness. Thin-walled structures are often applied for this purpose (e.g. in aerospace and civil engineering), because of their favorable (high) stiffness to mass ratio. It is well-known that thin-walled structures are liable to buckling and static buckling analysis is often carried out to assess their static stability. In many situations, additionally to the static load, a dynamic load is

This research is supported by the Dutch Technology Foundation STW, Applied Science Division of NWO and the Technology Programme of the Ministry of Economic Affairs (STW project EWO.5792).

R.H.B. Fey (✉) · H. Nijmeijer
Department of Mechanical Engineering, Eindhoven University of Technology, PO Box 513, 5600 MB Eindhoven, The Netherlands
e-mail: R.H.B.Fey@tue.nl

N.J. Mallon
TNO Built Environment and Geosciences, Centre for Mechanical and Maritime Structures, PO Box 49, 2600 AA Delft, The Netherlands

C.S. Kraaij
IHC Lagersmit BV, PO Box 5, 2960 AA Kinderdijk, The Netherlands

Published online: 09 February 2011

present, e.g. due to motions of the base of the structure. These situations require assessment of the dynamic stability of the structure. Especially excitation frequencies, which bring the structure into resonance, may induce dynamic buckling/instability (large motions and deformations) of the structure. This may lead to damage to the structure or even to total collapse of the structure.

In the literature, modeling and analysis for dynamic stability assessment of structures received increasing attention in the last decade. A well-known phenomenon, which may affect the dynamic stability of a structure, is the occurrence of parametric resonance. Good textbooks for studying the parametric resonance phenomenon and which can be used for dynamic stability assessment of structural elements such as beams, plates, and (cylindrical) shells are among others [1–3].

In this paper, nonlinear resonances in a coupled shaker-beam-top mass system are investigated both numerically and experimentally. The imperfect, vertical, slender beam carries a top mass and is coupled to and axially excited by the shaker at its base. The top mass can only move in vertical direction. The boundary conditions of the beam are clamped-clamped. A schematic overview of the system is given in Fig. 1. This can be seen as an archetype system for studying the dynamic stability of a load carrying, thin-walled structure. The weight of the top mass causes a compressive prestress, but is not large enough to cause static buckling. The harmonic base excitation, however, may induce dynamic buckling due to parametric and/or direct resonance.

In literature, not many papers consider parametric excitation of beams with a point mass attached to the beam. In [4, 5], the top mass is completely free in contrast to the situation in the current paper. In [6], parametric excitation of a horizontal, simply supported elastic beam with a point mass attached to one end is studied. This point mass can only move in horizontal direction. Initially, the geometry of the beam is perfectly straight and the beam is without static prestress. Parametric resonance motions are obtained using the method of multiple scales. Stability and bifurcations are investigated by considering the relation between response amplitude and excitation frequency and theoretical predictions are confirmed by experiments.

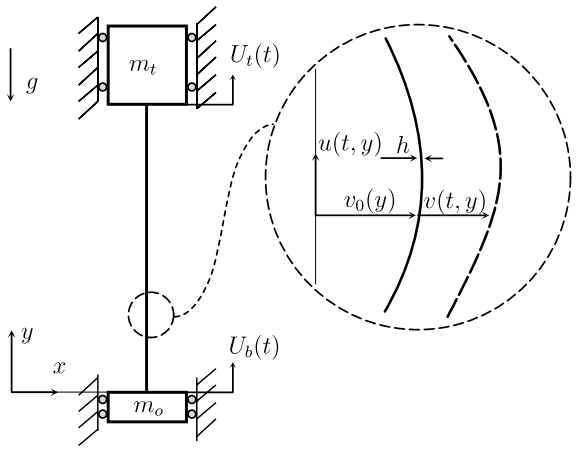

Fig. 1 Base-excited slender beam with top mass

In the current paper, a semi-analytical modeling approach is used resulting in a low-dimensional model. Geometric imperfections of the beam and linear as well as quadratic viscous damping are taken into account. The model also includes models of the amplifier and shaker used in the experiments. Advanced numerical tools are used for calculating branches of periodic solutions and their local stability and for bifurcation analysis. In combination with the low-dimensional semi-analytical model, these tools permit fast parameter studies. Single- and two-mode discretizations for the beam are considered in obtaining steady-state responses. Numerically obtained steady-state response results are validated by experiments.

The situation, where the weight of the top mass exceeds the static buckling load of the beam, although not discussed in the current paper, is certainly worthwhile mentioning from an application point of view. Namely, in this buckled situation, the beam may serve to dynamically isolate the top mass from the vibrating base, see [7, 8].

The outline of this paper is as follows. In the next section, the semi-analytical amplifier-shaker-structure model will be derived and discussed. In Sect. 3, the experimental set-up of the base-excited slender beam with top mass will be introduced. The steady-state response results, predicted by the semi-analytical approach and obtained experimentally, will be compared in Sect. 4. Finally, in Sect. 5, conclusions and recommendations will be presented.

2 Semi-analytical model

At the experimental set-up used, see Sect. 3, base excitation of the slender beam is realized by supplying an amplified harmonic input voltage to an electrodynamic shaker system. The resulting base acceleration will not be purely harmonic, will not have a constant amplitude but will be influenced by the dynamics of the shaker system carrying the slender beam with top mass. Response results for voltage excitation can thus not directly be compared with results for a prescribed harmonic base acceleration as considered in [9]. To be able to compare the experimental results with the semi-analytical results in a quantitative manner, the equations of motion for the base-excited slender beam with top mass will be coupled with a model of the shaker. The derivation of this coupled model is the topic of this section.

2.1 Modeling of the slender beam with top mass

Figure 1 shows the beam under consideration with length L, width b, and thickness h. The beam is very slender, i.e. $h \ll L$. Consequently, the displacements of the beam will be dominated by changes in curvature allowing to assume the beam to be inextensible. In addition, the slender beam is considered to be initially not perfectly straight. In the initial stress free state, the transversal shape of the slender beam is denoted by $v_0(y)$. The axial displacement field relative to the absolute axial base displacement $U_b(t)$ is indicated by $u(t, y)$ and the transversal displacement field relative to $v_0(y)$ by $v(t, y)$.

The length of an infinitesimally small piece of the beam in the initial state satisfies [10]

$$ds^2 = dy^2 + (v_{0,y}\, dy)^2. \tag{1}$$

Due to the inextensibility assumption, the length of ds remains constant. In the deformed state this length satisfies [10]

$$ds^2 = (dy + u_{,y}\, dy)^2 + \big([v_{0,y} + v_{,y}]dy\big)^2. \tag{2}$$

By combining (1) and (2), the following inextensibility constraint results:

$$u_{,y} = \sqrt{1 - 2v_{0,y}\, v_{,y} - v_{,y}^2} - 1. \tag{3}$$

In the adopted Cartesian coordinate system $[x, y]$, the centerline of the deformed imperfect beam is described by the curve $[X(t, y), Y(t, y)]$, where $X(t, y) = v_0(y) + v(t, y)$ and $Y(t, y) = y + U_b(t) + u(t, y)$. The exact curvature of this curve follows from [11]

$$\kappa = \frac{X(t,y)_{,y}\, Y(t,y)_{,yy} - X(t,y)_{,yy}\, Y(t,y)_{,y}}{(X(t,y)_{,y}^2 + Y(t,y)_{,y}^2)^{\frac{3}{2}}}, \tag{4}$$

and can be evaluated in terms of (derivatives of) $v_0(y)$ and $v(t, y)$ solely, after substitution of (3). It is assumed that, depending on the maximum deflection, the constraint (3) and the curvature (4) can be accurately approximated by their Taylor-series expansions in $v_{,y}$ and $v_{0,y}$ up to nth order with n sufficiently high. For example, the third-order expansions of (3) and (4) yield

$$u_{,y} = -v_{0,y}\, v_{,y} - \frac{1}{2} v_{,y}^2, \tag{5}$$

$$\kappa = \kappa_0 + v_{,yy} + \frac{1}{2}(v_{0,yy} + v_{,yy})v_{,y}^2 + v_{,yy}\, v_{0,y}\, v_{,y} - \frac{1}{2} v_{,yy}\, v_{0,y}^2, \tag{6}$$

where $\kappa_0 = v_{0,yy} - \frac{3}{2} v_{0,yy}\, v_{0,y}^2$ is (in this case) the third-order approximation of the initial curvature. Higher-order approximations include higher-order terms in $v_{,y}$ and $v_{0,y}$.

The kinematic boundary conditions for the transversal displacement field of the clamped-clamped beam, see Fig. 1, are

$$\begin{aligned} &v(t, 0) = v(t, L) = 0 \quad \text{and} \\ &v(t, 0)_{,\,y} = v(t, L)_{,\,y} = 0. \end{aligned} \tag{7}$$

Each of the following modes a priori obeys these conditions:

$$\begin{aligned} &v_i(y) = \cos\big[(i-1)\pi y/L\big] - \cos\big[(i+1)\pi y/L\big], \\ &\quad i = 1, 2, 3, \ldots \end{aligned} \tag{8}$$

Using these modes, the transversal displacement field is discretized as

$$v(t, y) = \sum_{i=1}^{N} Q_i(t) v_i(y), \tag{9}$$

where $Q_i(t)$ [m] are N generalized degrees of freedom (DOFs). In a similar fashion, the initial shape

of the beam, i.e. the geometric imperfection, is discretized as

$$v_0(y) = \sum_{i=1}^{N_e} \frac{1}{2} e_i h v_i(y), \tag{10}$$

where e_i are *dimensionless* imperfection parameters and $N_e \leq N$. After discretization of $v_0(y)$ and $v(t, y)$, the corresponding axial displacement field $u(t, y)$ can be computed by integrating an nth-order expansion of (3). Subsequently, the absolute axial displacement of the top mass, see Fig. 1, follows from

$$U_t(t) = U_b(t) + u(t, L). \tag{11}$$

Note that (in general) U_t depends in a nonlinear fashion on the DOFs Q_i.

The kinetic energy $\mathcal{T}_{\text{beam}}$ and the potential energy $\mathcal{V}_{\text{beam}}$ of the beam with top mass are determined by

$$\mathcal{T}_{\text{beam}} = \frac{1}{2}\rho A \int_0^L \dot{v}^2 \, dy + \frac{1}{2} m_t \dot{U}_t^2, \tag{12}$$

$$\mathcal{V}_{\text{beam}} = \frac{1}{2} E I \int_0^L (\kappa - \kappa_0)^2 \, dy + m_t g U_t, \tag{13}$$

where $A = bh$ is the cross-sectional area, $I = bh^3/12$ is the second moment of area, ρ is the mass density, E is the Young modulus of the beam, g is the acceleration due to gravity, and m_t is the top mass. Note that the axial and rotatory inertia of the beam are neglected, i.e. the case $\rho A l \ll m_t$ and $h/L \ll 1$ (as stated before) is considered. Damping of the beam is modeled by including a linear and a quadratic viscous damping force for each DOF Q_i: $F_d = -c_i \dot{Q}_i - c_{q,i} |\dot{Q}_i| \dot{Q}_i$, where c_i is the linear viscous damping constant and $c_{q,i}$ is the quadratic viscous damping constant for DOF Q_i. With respect to the damping of slender beams, addition of quadratic damping improves the agreement between theoretical and experimental results in many studies [5, 12, 13]. These generalized damping forces result in the following Rayleigh dissipation function

$$\mathcal{R}_{\text{beam}} = \sum_{i=1}^{N} \left(\frac{1}{2} c_i \dot{Q}_i^2 + \frac{1}{3} c_{q,i} \text{sign}(\dot{Q}_i) \dot{Q}_i^3 \right). \tag{14}$$

Energy and work expressions (12)–(14) will be used to derive the coupled shaker-structure model in Sect. 2.3.

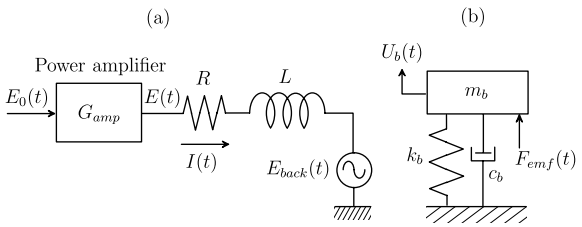

Fig. 2 Model of the electrodynamic shaker: (**a**) electrical part including amplifier, (**b**) mechanical part

2.2 Shaker model

The linear model of the electrodynamic shaker is depicted in Fig. 2, where the electrical part and the mechanical part are presented separately. Figure 2(a) shows the electrical part of the model including the power amplifier G_{amp}. Here, $I(t)$ represents the current, R the coil resistance, L the coil inductance, κ_c the current-to-force constant, and $E_{\text{back}}(t) = -\kappa_c \dot{U}_b(t)$ the back voltage. The power amplifier operates in voltage mode. More specifically, in the frequency domain

$$E(j\omega) = G_{\text{amp}}(j\omega) E_0(j\omega), \tag{15}$$

where $G_{\text{amp}}(j\omega)$ (with $j^2 = -1$) is a frequency dependent amplifier gain, E the harmonic output voltage and E_0 the harmonic input voltage.

Figure 2(b) shows the mechanical part of the model. The mass of the shaker armature m_b is a part of the total moving mass of the lower linear sledge m_o, see Fig. 1. The latter also includes the mass of the bottom clamping of the slender beam, see Sect. 3. The elastically suspended shaker armature mass is excited by the electromagnetic force $F_{\text{emf}}(t) = \kappa_c I(t)$ and is modeled as a single DOF structure with mass m_b, stiffness k_b, viscous damping c_b, and DOF U_b. It should be noted that for the mechanical modeling of the shaker, the shaker base is assumed to be rigidly connected to the fixed world. If this assumption is not followed, the resulting mechanical part of the shaker model would have more DOFs and unknown parameters to be identified, see for example [14].

The dynamics of the shaker are described by the two coupled ODEs [15]

$$\begin{aligned} L\dot{I} + RI + \kappa_c \dot{U}_b &= E(t), \\ m_b \ddot{U}_b + c_b \dot{U}_b + k_b U_b &= \kappa_c I + F_{\text{str}}, \end{aligned} \tag{16}$$

where the relation between E and E_0 in the frequency domain is given by (15). The force exerted to the

Table 1 Parameters of shaker model

c_b	278	[kg/s]	L	2.6×10^{-3}	[H]	P_{amp}	–88.3	[–]
m_b	3.0	[kg]	κ_c	11.5	[N/A]	b_{amp}	$1.4 \cdot 10^{-3}$	[s^{-1}]
k_b	5.28×10^4	[N/m]	R	0.9	[Ω]			

shaker mass by the structure it carries (the beam with top mass) is denoted by F_{str}, which in general depends on $\ddot{U}_b$, generalized DOFs Q_i, and their first and second time derivatives. The parameters of the shaker model are identified using frequency domain techniques, see [16] for more details. During the identification procedure of the unknown parameters of the shaker-amplifier system, the bare shaker was used, i.e. $F_{\text{str}} = 0$ [N]. A frequency dependency of the amplifier gain defined by

$$G_{\text{amp}}(j\omega) = P_{\text{amp}}(j\omega b_{\text{amp}} + 1), \tag{17}$$

is adopted to obtain a good fit of the shaker-amplifier dynamics for the frequency range of interest (0–300 [Hz]). Note that, using (17), the time domain version of (15) becomes

$$E(t) = P_{\text{amp}}\big(b_{\text{amp}}\dot{E}_0(t) + E_0(t)\big). \tag{18}$$

This equation can simply be substituted in (16). Note that E_0 is a known harmonic function of time. The identified parameter values for the shaker model are listed in Table 1.

Equation (16) can be written in first-order form based on the three states $I, U_b, \dot{U}_b$. In this way, a 3×3 system matrix, describing the dynamic properties of the bare shaker, is obtained. Using the parameter values from Table 1, the following three eigenvalues of the system matrix are found: $\lambda_1 = -278$ [rad/s] and $\lambda_2 = \bar{\lambda}_3 = -80.4 + 124\,j$ [rad/s]. Eigenvalue λ_1 is dominated by the properties of the electric circuit of the shaker. The imaginary parts of eigenvalues λ_2 and λ_3, corresponding to a damped eigenfrequency of $124/(2\pi) \approx 19.7$ [Hz], are dominated by the stiffness and mass of the shaker. The real parts of eigenvalues λ_2 and λ_3 are influenced by the mechanical damping as well as the properties of the electric circuit.

2.3 The coupled shaker-structure model

The coupled shaker-structure model will be derived by following a charge-displacement formulation of Lagrange's equations [17]. In this formulation, energy and work expressions of the coupled structure are formulated in terms of mechanical DOFs and (in this case) a single additional *charge* coordinate q. The first time derivative of q constitutes the current through the electrical part of the shaker model, i.e. $\dot{q} = I$.

The total set of $N + 2$ DOFs is collected in the column

$$\mathbf{Q}^* = [Q_1, \ldots, Q_N, U_b, q]^T, \tag{19}$$

where DOFs Q_i are the N generalized DOFs of the beam, see (9).

In the model of the slender beam, the axial motions are defined with respect to an arbitrary base motion U_b. For the coupled shaker/structure system, the energy/work expressions and the Rayleigh dissipation function now become

$$\begin{aligned}
\mathcal{M} &= \frac{1}{2}L\dot{q}^2 + \kappa_c \dot{q} U_b, \\
\mathcal{T} &= \mathcal{T}_{\text{beam}} + \frac{1}{2}m_o \dot{U}_b^2, \\
\mathcal{V} &= \mathcal{V}_{\text{beam}} + \frac{1}{2}k_b U_b^2, \\
\mathcal{R} &= \mathcal{R}_{\text{beam}} + \frac{1}{2}c_b \dot{U}_b^2 + \frac{1}{2}RI^2, \\
\delta\mathcal{W}_{nc} &= E(t)\delta q,
\end{aligned} \tag{20}$$

where $\mathcal{M}$ is the magnetic energy of the moving coil of the shaker and $\delta\mathcal{W}_{nc}$ is the virtual work done by the output voltage of the amplifier $E(t)$ [17]. Defining the Lagrangian $\mathcal{L}$ of the complete system by $\mathcal{L} = \mathcal{T} + \mathcal{M} - \mathcal{V}$, the final coupled set of equations of motion can be determined by

$$\frac{d}{dt}\mathcal{L}_{,\dot{\mathbf{Q}}^*} - \mathcal{L}_{,\mathbf{Q}^*} + \mathcal{R}_{,\dot{\mathbf{Q}}^*} = \mathbf{b}E(t), \tag{21}$$

where $\mathbf{b} = [0, \ldots, 0, 1]^T$ is an $N + 2$ dimensional column vector. Among others, this will lead to an explicit expression for F_{str}, the force exerted to the shaker mass by the slender beam with top mass, which was introduced in (16).

To illustrate some of the key features of the model, the equation of motion of the slender beam structure

is given for single-mode expansions of $v(t, y)$ and $v_0(y)$, i.e. $N = N_e = 1$ in (9)–(10), and using third-order Taylor-series approximations according to (5)–(6). This results in two ODEs for the shaker, see (16), which are coupled to the following single equation of motion for the beam with top mass

$$\begin{aligned} &M(Q_1)\ddot{Q}_1 + G(Q_1, \dot{Q}_1) + C(\dot{Q}_1) \\ &\quad + p_1\left[1 - r_0(1 + \ddot{U}_b/g) - p_2 e_1^2\right]Q_1 + K(Q_1) \\ &= p_3 e_1 r_0(1 + \ddot{U}_b/g), \end{aligned} \tag{22}$$

where

$$r_0 = \frac{m_t g}{P_c} \tag{23}$$

is the ratio between the static load due the weight of the top mass and the static Euler buckling load of the (perfect) beam ($P_c = 4\pi^2 EI/L^2$). Furthermore, $\ddot{U}_b$ is the base acceleration, which follows from (16).

In (22), the following abbreviations are used

$$\begin{aligned} &p_1 = \frac{8\pi^4 EI}{L^3}, \qquad p_2 = \frac{\pi^2 h^2}{4L^2}, \qquad p_3 = \frac{h}{2}p_1, \\ &M(Q_1) = \left[\frac{3}{2}\rho AL + \frac{m_t\pi^4}{L^2}\left(h^2 e_1^2 + 4he_1 Q_1 + 4Q_1^2\right)\right], \\ &C(\dot{Q}_1) = c_1\dot{Q}_1 + c_{q,1}|\dot{Q}_1|\dot{Q}_1, \\ &G(Q_1, \dot{Q}_1) = \frac{2m_t\pi^4}{L^2}\dot{Q}_1^2\left(he_1 + 2Q_1\right), \\ &K(Q_1) = \frac{2\pi^6 EI}{L^5}\left(8Q_1^3 + 9he_1 Q_1^2\right). \end{aligned} \tag{24}$$

As can be noted, due to the nonlinear equations (5)–(6), (22) contains inertia nonlinearities in $M(Q_1)\ddot{Q}_1$ if $m_t > 0$ and stiffness nonlinearities in $K(Q_1)$. For $e_1 = 0$, the inertia nonlinearities are of the softening type (mass increases for increasing $|Q_1|$), whereas the stiffness nonlinearities are of the hardening type (stiffness increases for increasing $|Q_1|$). C contains linear and quadratic dissipative forces. G contains centrifugal and Coriolis forces. Furthermore, Q_1 is excited by $\ddot{U}_b$ in a parametric manner and for $e_1 \neq 0$ also in a direct manner. In the static situation, for $e_1 = 0$, the linear stiffness term becomes negative for $r_0 > 1$, indicating that the trivial static solution $Q_1 = 0$ becomes unstable, if the static Euler buckling load is exceeded; note that this does not depend on the order of the Taylor-series expansion.

It should be noted that, depending on the mode considered and/or the relative weight of the added discrete mass, inertia nonlinearities can change resonances of the beam from hardening type to softening type, see [5, 12, 18].

2.4 Discretizations and parameter identification

In Sect. 4, experimental steady-state response results will be compared to results based on semi-analytical models. For this, two semi-analytical models will be used: a model based on a single-mode discretization of v and v_0 ($N = N_e = 1$, see (9) and (10)) and a model based on a two-mode discretization of v and v_0 ($N = N_e = 2$). Later on in this paper, these two models will be respectively referred to as the 1-MODE model (this beam model coupled to the shaker model actually has five states: $Q_1, \dot{Q}_1, U_b, \dot{U}_b, I$) and the 2-MODE model (this model has two additional states: $Q_2, \dot{Q}_2$). All numerical responses presented in this paper are based on models using third-order Taylor series expansions of the inextensibility constraint (3) and the curvature (4), i.e. (5)–(6). By considering higher-order expansions of the exact kinematics and a multi-mode discretization, it is shown in [9] that the third-order single-mode semi-analytical model can (to a large extent) accurately describe the first harmonic resonance and the first (large amplitude) 1/2 subharmonic resonance of the base-excited (initially unbuckled) slender beam. It is noted that for accurate steady-state response prediction of an initially buckled beam, in general higher-order approximations of the exact kinematics are required [19].

The semi-analytical models have a number of parameters, i.e. imperfection and damping parameters, which must be experimentally identified. In addition, to cope with small model errors, the Young modulus E is considered as a parameter to be identified. Consequently, the 1-MODE model has four unknown parameters (i.e. e_1, c_1, $c_{q,1}$, and E) and the 2-MODE model has seven unknown parameters (i.e. e_1, c_1, $c_{q,1}$, e_2, c_2, $c_{q,2}$, and E). The numerical values for these parameters are identified by fitting periodic solutions, calculated using the semi-analytical models, to measured periodic solutions using a weighted least-squares method. In this method, harmonic steady-state responses are used for 11 different excitation frequencies (i.e. for 35, 37, 55, 60, 67, 74, 77, 91, 103, 121, and 136 [Hz]) on stable parts of the harmonic branch,

see Sect. 4. In general, responses around resonances are useful to identify damping parameters, whereas low-amplitude solutions are useful to identify geometric imperfections. The identification results are robust; using different periodic solutions results in minor changes of the identified parameter values. More details on the applied identification procedure can be found in [20] and [21].

3 Experimental set-up

Both a picture and a schematic overview of the experimental set-up are depicted in Fig. 3. The base excitation of the slender, steel beam is realized by using an electrodynamic shaker system. The slender beam is clamped between two linear sledges with very low friction in axial direction. The linear sledge at the top side of the beam is based on air bearings. This sledge with clamping block acts as the rigid top mass m_t. The top mass can be increased by mounting additional masses on top of the upper linear sledge. At the bottom side of the beam, a linear sledge is realized by an elastic support mechanism based on folded leaf springs. This elastic support mechanism is included, since the shaker armature suspension has a very low rotational stiffness. The bottom linear sledge is mounted rigidly on top of the shaker. The moving mass of the lower linear sledge, including the mass of the bottom clamping block and the mass of the shaker armature, equals $m_o = 3.2$ [kg]. The beam used for the experiments is made of spring steel. The material and geometric properties of the beam are listed in Table 2. As stated before, note that the value for the Young modulus E later will be used as a parameter to be identified to account for (small) model errors. This will be discussed in more detail later. Obviously, the identified Young

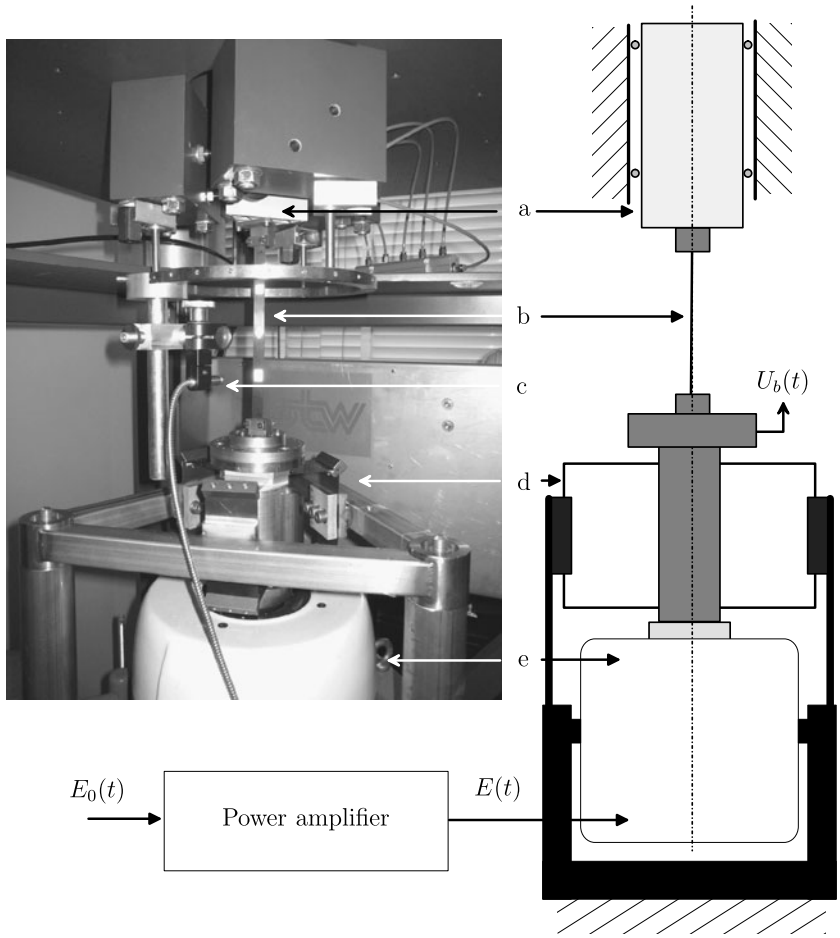

Fig. 3 Picture and schematic overview of the experimental set-up: (**a**) top linear sledge (top mass) based on air bearings, (**b**) slender beam, (**c**) laser vibrometer, (**d**) elastic support mechanism for the base, (**e**) electrodynamic shaker

Table 2 Material and geometrical properties of the slender steel beam

E^*	2.0×10^{11}	[N/m^2]
ρ	7850	[kg/m^3]
L	180	[mm]
b	15	[mm]
h	0.5	[mm]

$*$ this parameter will be further refined during the identification procedure with the experimental results

modulus should not differ too much from its well-known value for steel given in Table 2.

At the experimental set-up, the base excitation is introduced by supplying a harmonically varying input voltage

$$E_0(t) = v_d \sin(2\pi f t) \text{ [V]}, \tag{25}$$

to the power amplifier, where v_d is the voltage amplitude and $f = 1/T$ is the excitation frequency. The output voltage of the power amplifier $E(t)$, see Fig. 3, is supplied to the shaker. The amplifier works in a voltage mode of operation, i.e. the output voltage of the amplifier is kept proportional to its input voltage. No active feedback is used to control the acceleration of the base $\ddot{U}_b$. Consequently, the resulting acceleration of the shaker (and thus the effective axial force on the slender beam with top mass) will not be proportional to the input voltage $E_0(t)$ as given by (25), but will be influenced by the dynamics of the shaker system carrying the slender beam with top mass. Due this fact, it is essential to derive a coupled shaker/structure model to be able to compare numerical results with experimental results as has been done in Sect. 2.

A laser vibrometer (Ono Sokki LV 1500) is used to measure the transversal velocity ($\dot{v}$) at one point of the beam. In the static equilibrium state obtained for zero input voltage ($E_0 = 0$ [V]), the vibrometer is located at beam height $y = L/4$ (see Fig. 1). Note that y is measured relative to the base motion U_b. In the dynamic situation, the vibrometer measures the transversal velocity of the beam at a height $L/4 - U_{b,\text{dyn}}(t)$ relative to the static equilibrium position of the base, where $U_{b,\text{dyn}}(t)$ is the dynamic part of the base displacement caused by a non-zero input voltage E_0. The vibrometer was not mounted so as to follow the shaker movements, since the vibrometer is sensitive and susceptible to damage caused by vibrations. The signal of the laser vibrometer is numerically integrated to obtain measurements in terms of transversal displacements v. To avoid drift during the numerical integration, the measurement signal is filtered using a high pass filter with a cut-off frequency of 1.6 [Hz]. The data-acquisition and input signal generation is performed using a laptop with Matlab/Simulink in combination with a TUeDACS AQI.[1] A sample frequency of 4 [kHz] is used. Note that $U_{b,\text{dyn}}(t) \ll L/4$. Therefore, the experimentally observed transversal velocity and displacement at $L/4 - U_{b,\text{dyn}}$ may be compared to the numerically obtained signals $\dot{v}(t, L/4)$ and $v(t, L/4)$.

4 Steady-state response results

In this section, experimental steady-state response results for the base-excited slender beam with top mass will be compared with semi-analytical results obtained for the 1-MODE model and the 2-MODE model, see Sect. 2. The experimental steady-state results are obtained using harmonic excitation according to (25) for a constant voltage amplitude v_d and a stepwise varying excitation frequency $f = 1/T$. This procedure is called a stepped sine frequency sweep. For each case, a sweep-up (the excitation frequency is incrementally increased) and a sweep-down (the excitation frequency is incrementally decreased) is performed using a step size of $\Delta f = 0.5$ [Hz]. For each discrete value of f, the signals are saved during $N_e = 150$ excitation periods. The data during the first $N_t = 50$ periods are not used to minimize transient effects.

As explained before, the dynamic steady-state response of the beam is experimentally characterized using the measured velocity signal $\dot{V}_{L/4}(t) = \dot{v}(t, L/4 - U_{b,\text{dyn}})$, and its corresponding displacement signal $V_{L/4}(t) = v(t, L/4 - U_{b,\text{dyn}})$ obtained by filtering and numerical integration of $\dot{V}_{L/4}(t)$. Based on these two signals, the following averaged peak-to-peak amplitudes are determined

$$\tilde{\dot{V}}_{L/4} = \frac{1}{N_m} \sum_{k=0}^{N_m-1} \Big(\max_{T_m} \dot{v}_{(k)}(t, L/4 - U_{b,\text{dyn}}) - \min_{T_m} \dot{v}_{(k)}(t, L/4 - U_{b,\text{dyn}}) \Big), \tag{26}$$

[1] http://www.tuedacs.nl/, TUeDACS Advanced Quadrature Interface.

$$\tilde{V}_{L/4} = \frac{1}{N_m} \sum_{k=0}^{N_m-1} \Big(\max_{T_m} v_{(k)}(t, L/4 - U_{b,\mathrm{dyn}}) - \min_{T_m} v_{(k)}(t, L/4 - U_{b,dyn}) \Big), \tag{27}$$

where $T_m = (N_e - N_t)T/N_m$, T is the excitation period, $N_m = 5$ [-] is the number of records, and k refers to the kth record. Because $T_m = 20$, the peak-to-peak amplitude of a $1/20$th subharmonic solution still can be estimated. This is not possible anymore for subharmonic solutions with a period time longer than $20T$ and aperiodic solutions. Averaging is applied to cancel measurement noise to some extent.

Experimental steady-state results will be presented for two different beams (named **beam 1** and **beam 2**), which have the same dimensions and material properties (see Table 2), but have slightly different geometric imperfections and damping behavior, as will be illustrated. In this section, the numerical steady-state results for the 1-MODE and 2-MODE models are obtained using the software package AUTO97 [22], which is capable of: (1) calculating branches of periodic solutions of a nonlinear dynamic system for a varying system parameter, (2) analyzing the local stability of these branches using Floquet theory, and (3) detecting local bifurcations on these branches. More theoretical background on these topics can be found in [23]. Branches with stable periodic solutions will be plotted using solid lines, whereas branches with unstable periodic solutions will be plotted using dashed lines. Furthermore, cyclic fold bifurcations will be indicated by symbols 'o' and period doubling bifurcations will be indicated by symbols '$\diamond$'. Numerical peak-to-peak values equivalent to quantities defined in (26) and (27) are obtained as follows. In AUTO97, the equations of motion given by (21) are programmed in first-order form. This means that the periodic solutions are available in state space, i.e. in terms of $\mathbf{Q}^*$, see (19), and its first time derivative. By substituting DOFs Q_i in (9) and their first time derivatives in the first time derivative of (9), $v(t, L/4)$ and $\dot{v}(t, L/4)$ are obtained, from which directly the peak-to-peak values can be derived.

4.1 Steady-state responses for **beam 1**

In Fig. 4, the experimentally obtained frequency–amplitude plot (both in terms of dimensionless displacement $\tilde{V}_{L/4}/h$ [-] and velocity $\tilde{\dot{V}}_{L/4}$ [m/s]) is depicted by means of black dots for **beam 1** with $v_d = 0.03$ [V] and $m_t = 0.51$ [kg], i.e. $r_0 = 0.135$. Both frequency sweep-up and frequency sweep-down results are plotted. Experimentally, large frequency hysteresis intervals can be observed between 58–68 [Hz] and 92–142 [Hz]. In this figure, also steady-state response results are depicted based on the semi-analytic 1-MODE model. The identified parameter values for this case are listed in the first column of Table 3. As can be noted, the Young modulus E is identified to be a little bit lower than the theoretical value. This may be due to a combination of the following three facts: (1) in the set-up, the clamped-clamped boundary conditions will not be as ideal as considered in the model, (2) for the discretization of v, see (9), not the exact

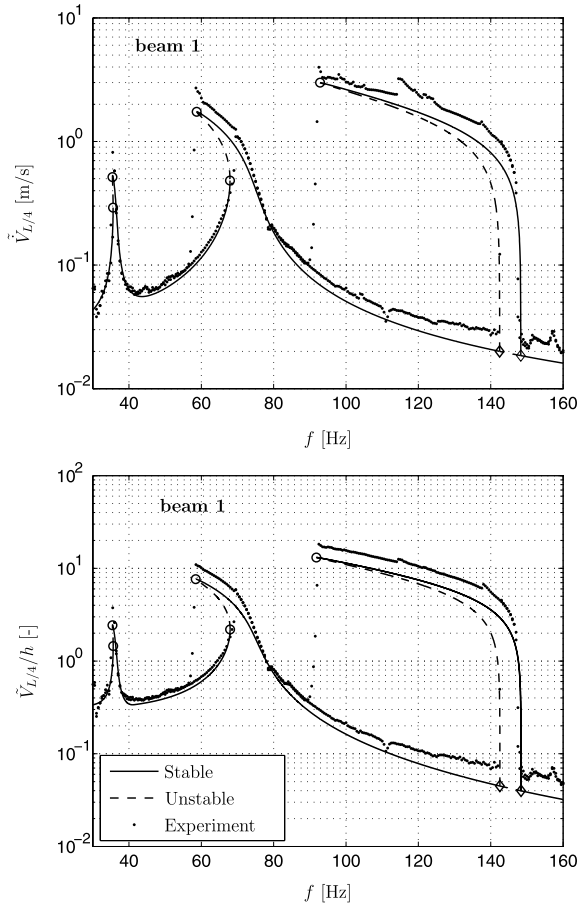

Fig. 4 Frequency–amplitude plot in terms of velocity $\tilde{\dot{V}}_{L/4}$ (*top*) and in terms of displacement $\tilde{V}_{L/4}/h$ (*bottom*) for **beam 1** with $v_d = 0.03$ [V] and $m_t = 0.51$ [kg] (experimental versus semi-analytical results based on 1-MODE model)

Table 3 Identified parameter values based on experimental results obtained for $v_d = 0.03$ [V] and $m_t = 0.51$ [kg]

Parameters	**beam 1**, 1-MODE	**beam 2**, 1-MODE	**beam 2**, 2-MODE
e_1 [–]	1.24	1.36	1.36
c_1 [Ns/m]	0.04	0.0	0.0
$c_{q,1}$ [kg/m]	0.20	0.20	0.2
e_2 [–]	–	–	0.04
c_2 [Ns/m]	–	–	0.04
$c_{q,2}$ [kg/m]	–	–	0.0
E [N/m^2]	1.92×10^{11}	1.95×10^{11}	1.95×10^{11}

Table 4 Eigenfrequencies f_i and damping ratios ξ_i of linearized models with parameters according to Table 3 and $m_t = 0.51$ [kg]

	beam 1, 1-MODE	**beam 2**, 1-MODE	**beam 2**, 2-MODE
f_1 [Hz]	18.1	18.1	18.1
ξ_1 [–]	0.489	0.489	0.489
f_2 [Hz]	72.7	73.1	73.1
ξ_2 [–]	0.0034	0.001	0.001
f_3 [Hz]	–	–	215.8
ξ_3 [–]	–	–	0.007

vibrational eigenmodes are used, which will result in a model, which overestimates the resonance frequencies, and (3) in the model, axial inertia and axial strain of the beam are not included, which may also result in a small overestimation of the resonance frequencies of the model.

For **beam 1**, the eigenfrequencies and damping ratios of the resulting 1-MODE model linearized around the static equilibrium position are listed in the first column of Table 4. The lowest eigenfrequency of the model (f_1) corresponds to a suspension mode of the shaker, i.e. the mode shape is dominated by U_b. This mode is highly damped (although still undercritically damped). The second eigenfrequency of the model (f_2) corresponds to the first bending mode of the beam, i.e. the mode shape is dominated by Q_1. This mode is very weakly damped.

Next, the obtained steady-state responses as depicted in Fig. 4 are discussed in more detail. The responses computed with the semi-analytical model show a second superharmonic resonance at $f \approx f_2/2$, a harmonic resonance at $f \approx f_2$, and a 1/2 subharmonic resonance (the latter branch contains periodic solutions with period $2T$). The first two resonances are caused by direct excitation, see the right-hand side of (22). The 1/2 subharmonic resonance is a parametric resonance, since it is caused by parametric excitation (in the expression for the linear stiffness, a periodic time dependent term is present), see (22). This parametric resonance is initiated at two period doubling bifurcations near $f = 2f_2$, which are indicated by two '$\diamond$' symbols. All three resonances show a softening type of behavior due to the inertia nonlinearities and are qualitatively similar as found for the case of a harmonic base acceleration, which is numerically investigated in [9]. Cyclic fold bifurcations are indicated by symbols 'o' and are found on all three resonance peaks.

The bifurcation points mark the boundaries for frequency hysteresis intervals. At these bifurcation points, large sudden jumps in the peak-to-peak values occur during the frequency sweep-up and the frequency sweep-down. The frequency hysteresis interval for the second superharmonic resonance near $f \approx f_2/2$ is very small because the frequencies, at which the two cyclic fold bifurcations occur, are very close to each other. The boundaries of the frequency hysteresis interval associated with the harmonic resonance are marked by cyclic fold bifurcations at 58 [Hz] (a jump occurs to the low-amplitude branch in the sweep-down) and 68 [Hz] (a jump occurs to the high-amplitude branch in the sweep-up). The boundaries of the frequency hysteresis interval associated with the 1/2 subharmonic (parametric) resonance are marked

by a cyclic fold bifurcation at 92 [Hz] (a jump occurs to the low-amplitude branch in the sweep-down) and a subcritical period doubling bifurcation at 142 [Hz] (a jump occurs to the high-amplitude branch in the sweep-up).

In the experimental sweep-up and sweep-down, at frequencies, where sudden jumps in the peak-to-peak values occur as explained above, sometimes experimental peak-to-peak values are visible in between the values for the high amplitude branch and the low-amplitude branch. Most clearly this is visible near 58 [Hz] and 92 [Hz] in the sweep-down. In theory, at these frequencies a discontinuous jump in the peak-to-peak value occurs. In the frequency sweep experiments, transient effects are the cause of these intermediate peak-to-peak values. Recall that in the experiment the frequency sweep is carried out stepwise and that each excitation frequency is kept constant for 150 periods, see the introduction of Sect. 4. For the determination of a peak-to-peak value in the experiment, for each excitation frequency only the last 100 periods are taken into account. For the frequencies corresponding to the intermediate peak-to-peak values, a number of 50 periods is apparently not high enough to let the transient damp out. Obviously, if the peak-to-peak value suddenly changes from 4 m/s to 0.1 m/s, such as in e.g. the sweep-down near 92 Hz, it takes some time before the transient has damped out. This phenomenon is also visible in the sweep-down near 58 Hz and even also for the sweep-up near 142 Hz (a single black dot is visible just above the 0.1 m/s line, almost coinciding with the vertically oriented dashed curve).

In this paper, the harmonic resonance is not significantly smaller than the subharmonic resonance in contrast to results found in [9]. This may be due to the fact that in the current paper, the amplitude of the base acceleration does not remain constant if the excitation frequency is varied. Especially near $f = f_1$ (not visible in Fig. 4), where the resonance related to the suspension mode of the shaker occurs, the base acceleration will show an increase in amplitude. Furthermore, the identified quadratic damping parameter $c_{q,1}$, see Table 3, is relative large with respect to the parameter values considered in [9]. During the parameter identification procedure it is found that inclusion of quadratic damping is essential to get good fit results, especially around the harmonic resonance and the 1/2 subharmonic resonance. The beneficial influence of the quadratic damping on the quality of the fit between numerical results and experimental results is also observed in [5, 12] and for cubic damping in [24].

In general, the experimental steady-state results are in good correspondence with the semi-analytical results. However, some discrepancies can be noted. First of all, the experimental results show a somewhat larger amplitude, especially in the peaks of the harmonic and the subharmonic resonance (both in terms of $\tilde{\dot{V}}_{L/4}$ [m/s] and $\tilde{V}_{L/4}/h$ [-]). Furthermore, the experimentally obtained frequency–amplitude plots show at a number of (small) frequency regions, small peaks and/or small jumps, which are not present in the semi-analytical results. These peaks can be most clearly observed in the frequency–amplitude plot in terms of $\tilde{\dot{V}}_{L/4}$ [m/s] (see upper plot of Fig. 4), for example near the top of the harmonic resonance ($f \approx 60$ [Hz]) and along the subharmonic resonance branch near $f = 120$ [Hz]. More comments on these peaks will be given at the end of this section. From now on, the frequency–amplitude plots will only be presented in terms of $\tilde{\dot{V}}_{L/4}$ [m/s], since from these plots details in the steady-state responses can be distinguished best.

As stated before, the imperfection and damping parameters of the 1-MODE model for **beam 1** are identified using the experimental response obtained for $v_d = 0.03$ [V] and $m_t = 0.51$ [kg]. For further validation, the response predicted by this model is compared with experimental results for a higher excitation amplitude, i.e. $v_d = 0.04$ [V], see the upper plot of Fig. 5, and for a larger top mass, i.e. $m_t = 1.01$ [kg], see the lower plot of Fig. 5. Except for the fact that for $v_d = 0.04$ [V], the 1/2 subharmonic branch of the semi-analytical model continues to a lower excitation frequency, the semi-analytical results are in this case again in good correspondence with the experimental results. For $m_t = 1.01$ [kg], both the 1/2 subharmonic resonance and the harmonic resonance of the semi-analytical model continue to lower excitation frequencies than observed in the experimental results. In this sense, the nonlinear damping characteristics, identified for one load case, cannot predict exactly the damping characteristics for another load case (the amount of overhang of the resonance curves is mainly influenced by the damping parameters). Nevertheless, for both cases shown in Fig. 5, the semi-analytical results based on the 1-MODE model are in satisfactory correspondence with the experimental results.

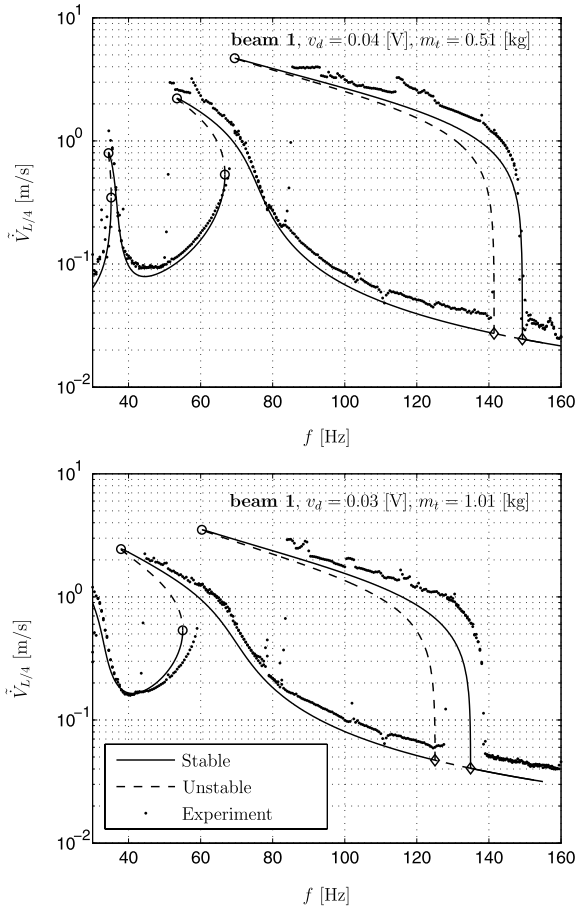

Fig. 5 Frequency–amplitude plots for increased excitation amplitude (*top*) and increased top mass (*bottom*) (experimental versus semi-analytical results based on 1-MODE model for **beam 1**)

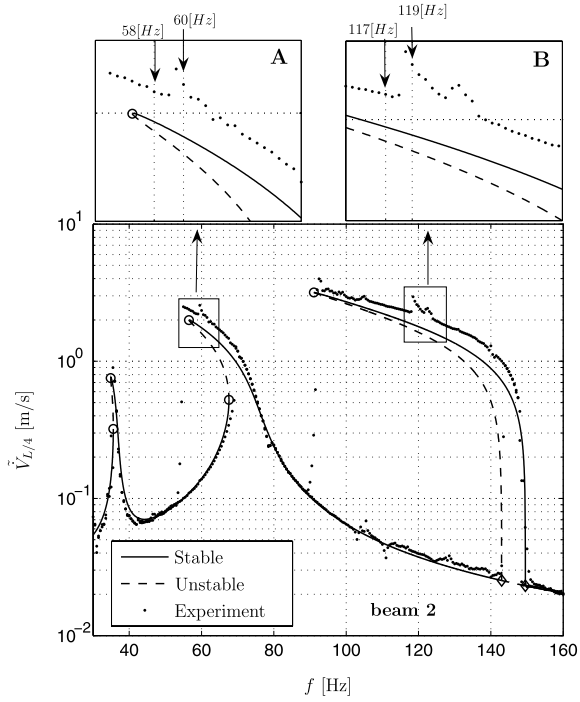

Fig. 6 Frequency–amplitude plot for **beam 2** with $v_d = 0.03$ [V] and $m_t = 0.51$ [kg] (experimental versus semi-analytical results based on 1-MODE model)

4.2 Steady-state responses for beam 2

For **beam 2**, experimental steady-state results will first be compared with results for the 1-MODE model and subsequently with results for the 2-MODE model, see Sect. 2. For the 1-MODE model, the identified parameter values are listed in the second column of Table 3. The eigenfrequencies and damping ratios of the resulting 1-MODE model for **beam 2** (again linearized around the static equilibrium position) are listed in the second column of Table 4. For the largest part, the identified parameter values are comparable to those obtained for **beam 1**. However, now the linear damping coefficient c_1 is identified zero. Note that this does not result in a zero damping ratio for the first beam mode f_2 (see Table 4), since this mode has some (linear) coupling with the heavily damped suspension mode of the shaker.

In Fig. 6, the experimentally obtained frequency–amplitude plot and the corresponding 1-MODE model response are depicted for **beam 2** for the same loading conditions as considered for **beam 1** in Fig. 4 ($v_d = 0.03$ [V], $m_t = 0.51$ [kg]). Similar to Fig. 4, also in Fig. 6 the steady-state response results based on the 1-MODE model are in good correspondence with the experimental results. Furthermore, in addition to the three large resonance peaks, also in this frequency–amplitude plot small resonance peaks (and associated small jumps) can be noted in small frequency ranges. Again a very clear (small) jump occurs near the top of the harmonic resonance near $f = 60$ [Hz] and another one along the subharmonic resonance branch near $f = 120$ [Hz], see enlargements **A** and **B** in Fig. 6. Projections of the experimental response on the phase plane spanned by $V_{L/4}(t)$ and $\dot{V}_{L/4}(t)$ and the corresponding Poincaré mappings, i.e. period T sampled values of $V_{L/4}$ plotted against period T sampled values of $\dot{V}_{L/4}$, close to these two jumps, are depicted in Fig. 7. At $f = 58$ [Hz], at the left side of the jump, see enlargement **A** in Fig. 6, the Poincaré map shows a sin-

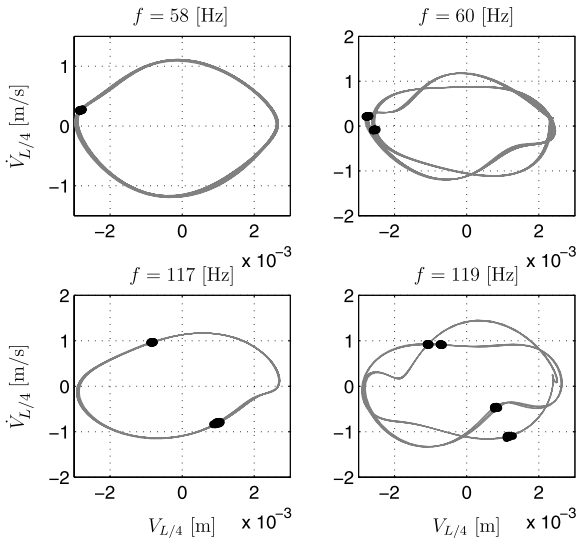

Fig. 7 Phase-plane projections and Poincaré mappings for four experimentally obtained responses for **beam 2** with $v_d = 0.03$ [V] and $m_t = 0.51$ [kg]

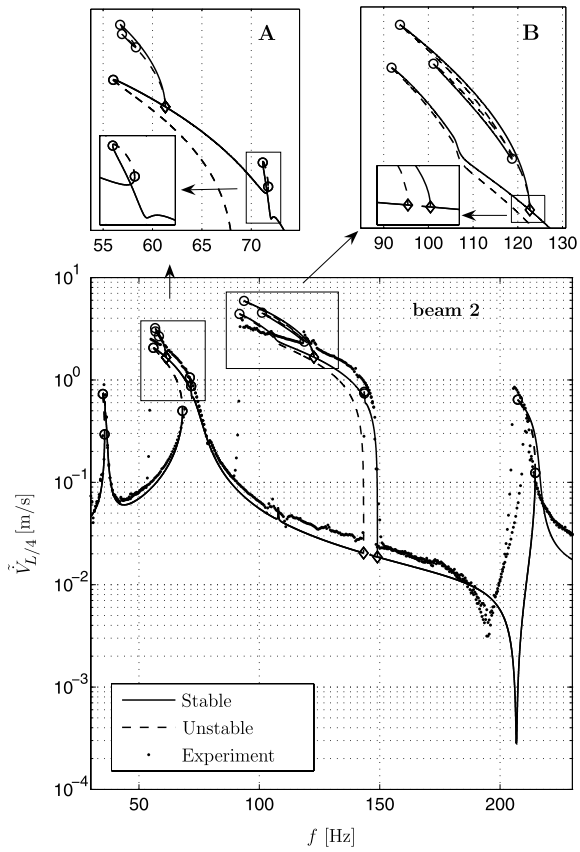

Fig. 8 Frequency–amplitude plot for **beam 2** with $v_d = 0.03$ [V] and $m_t = 0.51$ [kg] (experimental versus semi-analytical results based on 2-MODE model)

gle dot, indicating a harmonic response. However, at $f = 60$ [Hz], at the right side of the jump, see enlargement **A** in Fig. 6, the Poincaré map shows two dots, indicating a 1/2 subharmonic response. Similarly, for the scenario depicted in enlargement **B** in Fig. 6, for $f = 117$ [Hz] the response is 1/2 subharmonic and for $f = 119$ [Hz] the response has become 1/4 subharmonic.

These additional small branches with subharmonic responses are not captured by the 1-MODE model. To examine if the experimentally observed period doubling behavior is due to nonlinear interaction with the second beam mode v_2, a semi-analytical model with two beam modes (the 2-MODE model) is derived, see Sect. 2. In Fig. 8, the steady-state response predicted by the 2-MODE model is compared with experimental results obtained for **beam 2** and $v_d = 0.03$ [V] and $m_t = 0.51$ [kg] (same values as used in Fig. 6). The experimental results in Figs. 6 and 8 are obviously identical. The identified parameter values are listed in the last column of Table 3 and the eigenfrequencies and damping ratios of the 2-MODE model linearized around the static equilibrium position are listed in the last column of Table 4. A very small geometric imperfection related to the second bending mode of the beam is identified: $e_2 = 0.04$ [-]. In the parameter identification for the second mode no quadratic damping is found, i.e. $c_{q,2} = 0$ [kg/m].

As can be noted in Fig. 8, inclusion of the second beam mode in the model instigates a second harmonic resonance with softening around $f = 215$ [Hz]. This second harmonic resonance is observed at a slightly lower frequency in the experimental results. Furthermore, and in correspondence with the experimental results, in the semi-analytical results for the 2-MODE model at the 1/2 subharmonic branch near $f = 123$ [Hz], two period doubling bifurcations (indicated by two '◇' symbols) resulting in a branch with 1/4 subharmonic responses are observed, see enlargement **B** in Fig. 8. Note that for clarity no experimental results are shown in the enlargements. The 1/4 subharmonic branch itself exhibits three cyclic fold bifurcations resulting in two (separate) stable parts of the branch. Due to its complexity, this branch cannot be easily compared with the experimental results in this region, see the experimental results depicted in enlargement **B** of Fig. 6 (here only results for a frequency sweep-

down are shown). Nevertheless, it can be noted that for the semi-analytical results, the 1/4 subharmonic response continues to a lower excitation frequency as observed experimentally. This larger overhang is possibly due to the fact that in the semi-analytical model for the second mode no quadratic damping is taken into account. A similar phenomenon occurs in the top of the first harmonic resonance. Again in correspondence with the experimental results, near $f = 61$ [Hz] two nearly coinciding period doubling bifurcations occur (again indicated by two '$\diamond$' symbols), from which now a 1/2 subharmonic branch bifurcates, see enlargement **A**.

Furthermore, in the semi-analytical results near $f = 72 \approx f_3/3$ [Hz], see enlargement **A** in Fig. 8, a small 3rd superharmonic resonance can be distinguished, which is related to the second beam mode with eigenfrequency f_3, see the last column of Table 4. This superharmonic resonance cannot be seen in the experimental results. However, the frequency interval, in which this resonance occurs, is so small that it is possibly missed in the frequency sweep due to a too coarse frequency step. Subsequently, a very small 2nd superharmonic resonance related to the second beam mode can be observed near $f = 108 \approx f_3/2$ [Hz], both on the high-amplitude 1/2 subharmonic branch and on the low-amplitude harmonic branch. This resonance can be seen more clearly in the semi-analytical response than in the experimental response. Finally, a very small resonance can be seen on the 1/2 subharmonic branch near $f = 144 \approx 2f_3/3$ [Hz]. Two cyclic fold bifurcations associated with this resonance are indicated by 'o' symbols. Also here, this resonance can be seen more clearly in the semi-analytical response than in the experimental response.

For further validation, power spectral densities (PSDs) of the experimentally and semi-analytically obtained transversal velocities, i.e. $\dot{V}_{L/4}(t)$ and $\dot{v}(t, L/4)$, are compared in Fig. 9 for $f = 58$ [Hz] and $f = 60$ [Hz], and in Fig. 10 for $f = 117$ [Hz] and $f = 119$ [Hz]. In these PSD plots, the dimensionless frequency axis of the PSD F/f is normalized by the excitation frequency f. For the semi-analytical results, which are based on the 2-MODE model, the locations of the eigenfrequencies corresponding to the first two bending modes of the beam, i.e. f_2 and f_3 (see the last column of Table 4), are indicated. Recall that the experimental responses corresponding to these four excitation frequencies were also plotted in Fig. 7. First, consider Fig. 8 showing the PSDs of the harmonic response at $f = 58$ [Hz] and the 1/2 subharmonic response at $f = 60$ [Hz]. At $f = 58$ [Hz], frequency contributions to the harmonic response can be found at $F/f \in \{1, 2, 3, \ldots\}$. The harmonic resonance of the first beam mode is clearly indicated by a dominating contribution at $F/f = 1 \approx f_2/f$. At $f = 60$ [Hz], frequency contributions to the 1/2 subharmonic response can be found at $F/f \in \{\frac{1}{2}, 1, \frac{3}{2}, 2, \frac{5}{2}, \ldots\}$. The contribution of the first beam mode is still dominating at $F/f = 1 \approx f_2/f$, but a very important contribution of component $F/f = \frac{7}{2} \approx f_3/f$ has (suddenly) appeared, which obviously is missing in the PSD of the harmonic response at $f = 58$ Hz. This can be observed for the semi-analytical response as well as for the experimental response. It can be concluded that at $f = 60$ [Hz] an internal resonance is found, which is caused by nonlinear interaction between the first and second beam mode. A similar phenomenon can be seen in Fig. 10. At $f = 117$ [Hz], frequency contributions to the 1/2 subharmonic response can be found at $F/f \in \{\frac{1}{2}, 1, \frac{3}{2}, 2, \frac{5}{2}, \ldots\}$. The 1/2 subharmonic resonance of the first beam mode is clearly indicated by a dominating contribution at $F/f = \frac{1}{2} \approx f_2/f$. At $f = 119$ [Hz], frequency contributions to the 1/4 subharmonic response can be found at $F/f \in \{\frac{1}{4}, \frac{1}{2}, \frac{3}{4}, 1, \ldots\}$. The contribution of the first beam mode is still dominating at $F/f = \frac{1}{2} \approx f_2/f$, but in addition a very important contribution of component $F/f = \frac{7}{4} \approx f_3/f$ has (suddenly) appeared, which obviously is missing in the PSD of the 1/2 subharmonic response at $f = 117$ Hz. This can again be observed for the semi-analytical response as well as for the experimental response. Also at $f = 119$ [Hz] it can be concluded that an internal resonance is found, which is again caused by nonlinear interaction between the first and second beam mode. It is of interest to note that a two-to-seven internal resonance between the first two beam bending modes is also observed experimentally in [25].

In conclusion, the 2-MODE model can qualitatively explain the experimentally observed small extra resonances and period doubling behavior at the top of the first harmonic resonance and on the 1/2 subharmonic branch. For a better quantitative match of these (and other) dynamic response details, the damping and imperfection parameters of the model may need to be further refined and, possibly, also more beam modes must be included in the model. Moreover, more detailed experiments based on smaller frequency sweep

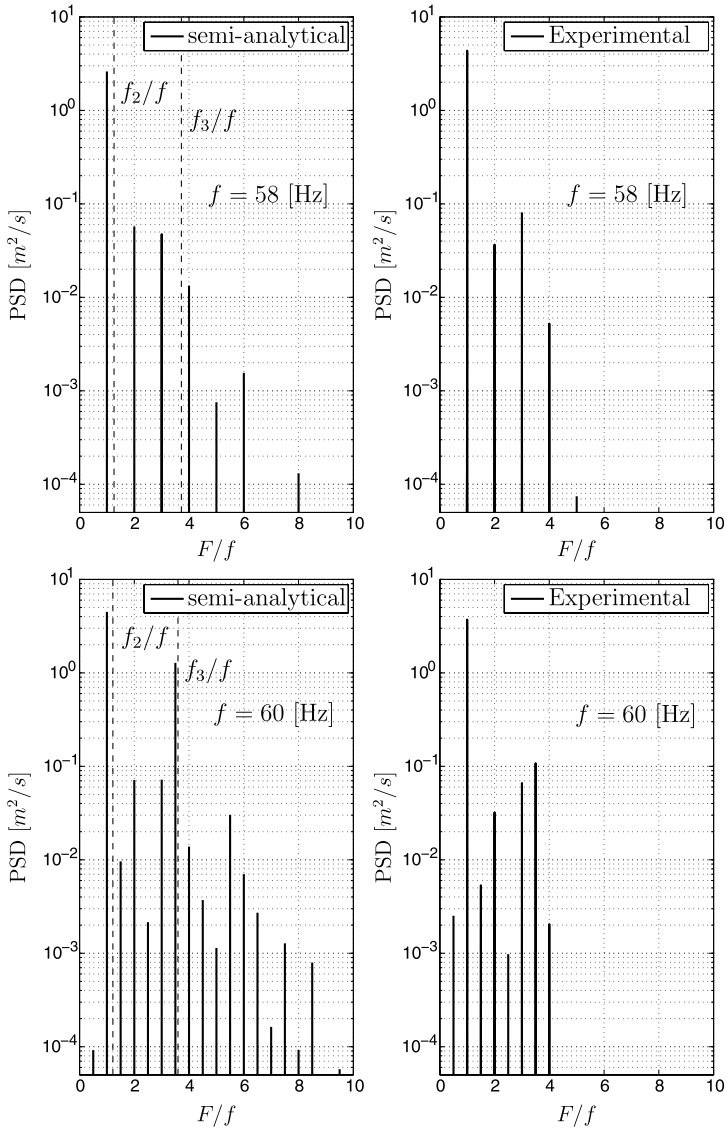

Fig. 9 Power Spectral Density of the response (semi-analytical results based on 2-MODE model versus experimental results) obtained for **beam 2** with $v_d = 0.03$ [V], $m_t = 0.51$ [kg], $f = 58$ [Hz] (*top*) and $f = 60$ [Hz] (*bottom*)

increments Δf may be necessary for (improved) identification of the (additional) damping and imperfection parameters. This, however, is considered to be out of the scope of this paper. Nevertheless, it has been illustrated that, using a semi-analytical approach, the steady-state dynamic response can be studied in detail.

5 Conclusions and recommendations

In this paper, the dynamic stability of a slender beam carrying a top mass has been investigated. The weight of the top mass is well below the static buckling load. The beam is dynamically excited at its base by means of an amplifier-shaker system with a harmonic input voltage.

A semi-analytical model has been derived for a base-excited slender beam carrying a top mass. The beam has been assumed to be inextensible. The nonlinear inextensibility constraint as well as the nonlinear expression for the curvature of the beam have been approximated by third-order Taylor-series expansions. In the model, geometrical imperfections of the beam have been taken into account. Furthermore, the beam model includes linear as well as quadratic viscous damping forces. This structural model has been extended by

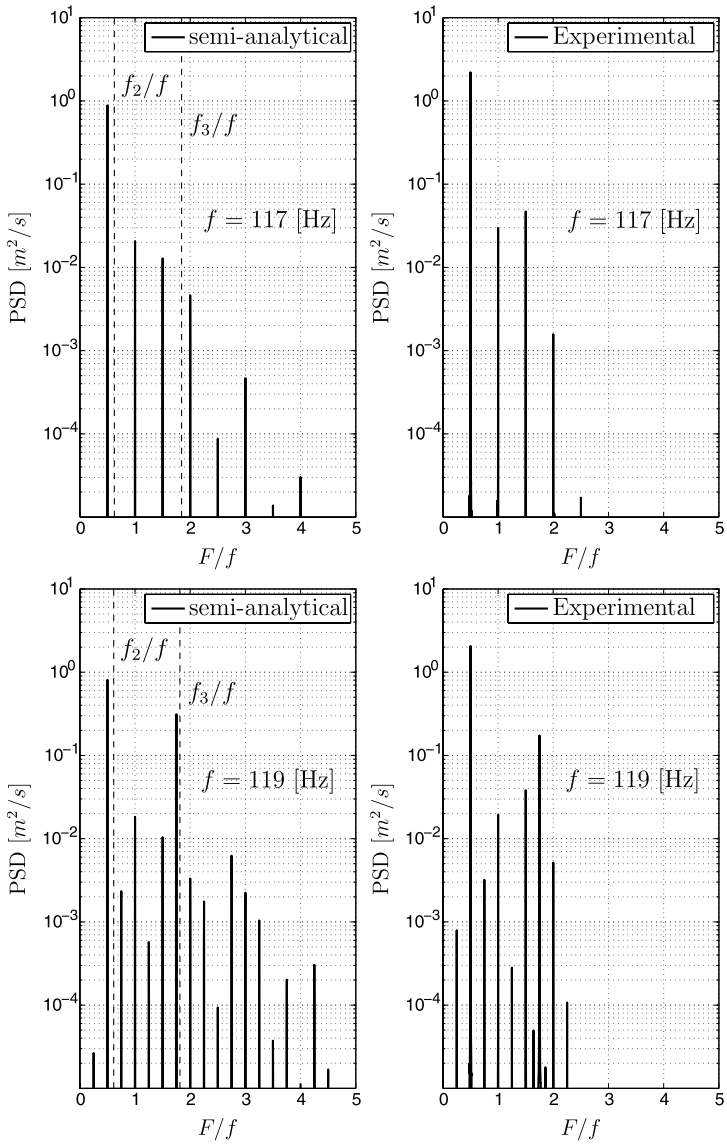

Fig. 10 Power Spectral Density of the response (semi-analytical results based on 2-MODE model versus experimental results) obtained for **beam 2** with $v_d = 0.03$ [V], $m_t = 0.51$ [kg], $f = 117$ [Hz] (*top*) and $f = 119$ [Hz] (*bottom*)

coupling it to a linear model of the shaker (with amplifier).

The resulting low-dimensional coupled model has been combined with numerical tools for efficient calculation of branches of steady-state solutions of the system and their local stability, and for detection of bifurcation points on these branches.

An experimental set-up has been built and used to validate the numerically obtained steady-state responses. In the experiments, frequency sweep-up and sweep-down has been performed with respect to the harmonic excitation voltage. Shaker and amplifier parameters have been identified experimentally for the bare amplifier-shaker system. Damping and imperfection parameters of the semi-analytical model have been identified by using a least-squares method, which fits numerically obtained periodic solutions as good as possible to experimentally obtained periodic solutions.

Frequency–amplitude curves have been calculated for both one-mode and two-mode discretizations of the beam. For the one-mode discretization, already a good match between numerical and experimental steady-state responses is obtained. The main resonances being a parametric 1/2 subharmonic resonance, a harmonic resonance, and a second superharmonic reso-

nance (all related to the first beam mode) are predicted well. Also the frequencies, at which (period doubling and cyclic fold) bifurcations are calculated, correspond well with the frequencies, at which experimentally sudden jumps in the response amplitude are observed during the frequency sweep-up and sweep-down. The two-mode model shows some additional resonances. Next to the (expected) second harmonic resonance also some smaller resonances (and extra bifurcations associated with these resonances) occur in the low-frequency range. Some of these resonances can be identified as combination resonances of the two beam modes. These additional resonances are also found in the experiments.

The results presented in this paper in principle only refer to the coupled shaker-beam system and therefore depend on the particular shaker used. The input voltage is harmonic with constant amplitude, but, since the system is nonlinear, the shaker force is not purely harmonic and has frequency dependent amplitude. The shaker dependency can be avoided by ensuring harmonic forcing at constant amplitude at different excitation frequencies by using a feedback controlled shaker. It is important to note, however, that the nonlinear resonance phenomena presented in the current paper still occur if the bottom of the beam is harmonically excited with constant amplitude. This is demonstrated by simulations in references [9, 16]. To some extent, this is not really a surprise, since the shaker dynamics are linear. Moreover, the resonance frequency (at 18.1 Hz) of the mode, where the shaker vibration dominates, is clearly below the interesting frequency range for the beam carrying the top mass (30–160 Hz). One could say that the shaker has been 'designed' in such a way that its dynamics does not qualitatively alter the dynamics of the beam carrying the top mass with harmonic base excitation.

As already concluded, good agreements with experiments were obtained with only one or two simple assumed modes for the beam. Therefore, as a suggestion for future research, analytical approximations for the frequency–amplitude curves might be attainable, using e.g. a perturbation method. At least this could give simple analytical expressions for the backbone curves (no damping or forcing) of the frequency–amplitude curves, providing the important relation between free oscillation frequency and amplitude.

Open Access This article is distributed under the terms of the Creative Commons Attribution Noncommercial License which permits any noncommercial use, distribution, and reproduction in any medium, provided the original author(s) and source are credited.

References

1. Nayfeh, A., Pai, P.: Linear and Nonlinear Structural Mechanics. Wiley-VCH, Weinheim (2004)
2. Virgin, L.: Vibration of Axially Loaded Structures. Cambridge University Press, New York (2007)
3. Amabili, M.: Nonlinear Vibrations and Stability of Shells and Plates. Cambridge University Press, Cambridge (2008)
4. Zavodney, L., Nayfeh, A.: The non-linear response of a slender beam carrying a lumped mass to a principal parametric excitation: theory and experiment. Int. J. Non-Linear Mech. **24**(2), 105–125 (1989)
5. Yabuno, H., Ide, Y., Aoshima, N.: Nonlinear analysis of a parametrically excited cantilever beam (effect of the tip mass on stationary response). JSME Int. J. Ser. B Fluids Therm. Eng. **41**(3), 555–562 (1998)
6. Son, I.-S., Uchiyama, Y., Lacarbonara, W., Yabuno, H.: Simply supported elastic beams under parametric excitation. Nonlinear Dyn. **53**, 129–138 (2008)
7. Winterflood, J., Barber, T., Blair, D.: Using Euler buckling springs for vibration isolation. Class. Quantum Gravity **19**(7), 1639–1645 (2002)
8. Virgin, L., Davis, R.: Vibration isolation using buckled struts. J. Sound Vib. **260**, 965–973 (2003)
9. Mallon, N., Fey, R., Nijmeijer, H.: Dynamic stability of a base-excited thin beam with top mass. In: Proc. of the 2006 ASME IMECE, Nov. 5-10, Paper 13148, pp. 1–10, Chicago, IL (2006)
10. Mettler, E.: Dynamic buckling. In: Flügge, W. (ed.) Handbook of Engineering Mechanics. McGraw-Hill, New York (1962)
11. Gibson, C.: Elementary Geometry of Differentiable Curves: An Undergraduate Introduction. Cambridge University Press, Cambridge (2001)
12. Anderson, T., Nayfeh, A., Balachandran, B.: Experimental verification of the importance of the nonlinear curvature in the response of a cantilever beam. J. Vib. Acoust. **118**(1), 21–27 (1996)
13. Yabuno, H., Okhuma, M., Lacarbonara, W.: An experimental investigation of the parametric resonance in a buckled beam. In: Proceedings of the ASME DETC'03, pp. 2565–2574, Chicago, IL (2003)
14. Xu, X., Pavlovskaia, E., Wiercigroch, M., Romeo, F., Lenci, S.: Dynamic interactions between parametric pendulum and electro-dynamical shaker. Z. Angew. Math. Mech. **87**(2), 172–186 (2007)
15. McConnell, K.: Vibration Testing, Theory and Practice. Wiley, New York (1995)
16. Mallon, N.: Dynamic stability of thin-walled structures: a semi-analytical and experimental approach. Ph.D. thesis, Eindhoven University of Technology (2008)
17. Preumont, A.: Mechatronics, Dynamics of Electromechanical and Piezoelectric Systems. Springer, Berlin (2006)
18. Atluri, S.: Nonlinear vibrations of a hinged beam including nonlinear inertia effects. J. Appl. Mech. **40**(1), 121–126 (1973)

19. Noijen, S., Mallon, N., Fey, R., Nijmeijer, H., Zhang, G.: Periodic excitation of a buckled beam using a higher order semi-analytic approach. Nonlinear Dyn. **50**(1–2), 325–339 (2007)
20. Kraaij, C.: A semi-analytical buckling approach: modeling and validation. Tech. Rep. DCT 2008.095, Eindhoven University of Technology (2008)
21. Verbeek, G., de Kraker, A., van Campen, D.: Nonlinear parametric identification using periodic equilibrium states. Nonlinear Dyn. **7**, 499–515 (1995)
22. Doedel, E., Paffenroth, R., Champneys, A., Fairgrieve, T., Kuznetsov, Y., Oldeman, B., Sandstede, B., Wang, X.: AUTO97: Continuation and bifurcation software for ordinary differential equations (with HOMCONT), Technical Report, Concordia University (1998)
23. Thomsen, J.: Vibrations and Stability; Advanced Theory, Analysis, and Tools, 2nd edn. Springer, Berlin (2003)
24. Zaretzky, C., da Silva, M.C.: Experimental investigation of non-linear modal coupling in the response of cantilever beams. J. Sound Vib. **174**(2), 145–167 (1994)
25. Ribeiro, P., Carneiro, R.: Experimental detection of modal interactions in the non-linear vibration of a hinged-hinged beam. J. Sound Vib. **277**(4–5), 943–954 (2004)